


## Article

# Impact Analysis of Super Typhoon 2114 ‘Chanthu’ on the Air Quality of Coastal Cities in Southeast China Based on Multi-Source Measurements

Fei Li <sup>1,2</sup> , Qiuping Zheng <sup>2</sup>, Yongcheng Jiang <sup>2</sup>, Aiping Xun <sup>2</sup>, Jieru Zhang <sup>3</sup>, Hui Zheng <sup>2</sup> and Hong Wang <sup>4,5,\*</sup>

<sup>1</sup> School of Atmospheric Sciences, Sun Yat-Sen University, Zhuhai 519082, China; leefeicat@163.com

<sup>2</sup> Xiamen Key Laboratory of Straits Meteorology, Xiamen Meteorological Bureau, Xiamen 361012, China; qp\_zheng@163.com (Q.Z.); ycjiaang@nuist.edu.cn (Y.J.); xunaiping@foxmail.com (A.X.); zhhui\_zoly@163.com (H.Z.)

<sup>3</sup> Xiamen Environmental Monitoring Station, Xiamen 361012, China; joremo@126.com

<sup>4</sup> Fujian Key Laboratory of Severe Weather, Fuzhou 350007, China

<sup>5</sup> China Meteorological Administration Straits Severe Weather Key Laboratory, Fuzhou 350007, China

\* Correspondence: wh1575@163.com

**Abstract:** The northward typhoon configuration along the southeast coast of China (TC<sub>N-SEC</sub>) is one of the key circulation patterns influencing the coastal cities in southeast China (CCSE). Here, we analyzed the air quality in CCSE during the high-incidence typhoon period from 2019 to 2021. Multi-source measurements were carried out to explore the impact of super typhoon 2114 ‘Chanthu’ on the air quality in CCSE. The results showed that the TC<sub>N-SEC</sub> and its surrounding weather situation had a favorable impact on the increase in pollutant concentration in CCSE, especially on the increase in O<sub>3</sub> concentration. From 13 September to 17 September 2021, affected by the cyclonic shear in the south of super typhoon 2114 ‘Chanthu’, the strong wind near the ground, stable relative humidity, strong precipitation, and the significantly reduced wind speed had a substantial effect on PM<sub>10</sub>, PM<sub>2.5</sub>, SO<sub>2</sub>, and NO<sub>2</sub> concentrations. Calm and light air near the ground, weak precipitation, high daily maximum temperatures, and minimum relative humidity may provide favorable meteorological conditions for the accumulation of O<sub>3</sub> precursors and photochemical reactions during the day, resulting in the daily peak values of O<sub>3</sub> exceeding 160 µg/m<sup>3</sup>. The evolution of wind, relative humidity, and boundary layer height could play an important role in the variations in PM<sub>10</sub> and PM<sub>2.5</sub> concentrations by influencing pollutant accumulation or diffusion. It was suggested that the atmospheric structure of horizontal stability and vertical mixing below 1500 m could play a significant role in the accumulation and vertical distribution of ozone. The results highlight the important role of typhoons in the regional environment and provide a scientific basis for further application of multi-source observation data, as well as air pollution control.

**Keywords:** wind profile; relative humidity; depolarization ratio; extinction coefficient and ozone; atmospheric diffusion condition; height of pollution boundary layer; coastal cities in southeast China



**Citation:** Li, F.; Zheng, Q.; Jiang, Y.; Xun, A.; Zhang, J.; Zheng, H.; Wang, H. Impact Analysis of Super Typhoon 2114 ‘Chanthu’ on the Air Quality of Coastal Cities in Southeast China Based on Multi-Source Measurements. *Atmosphere* **2023**, *14*, 380. <https://doi.org/10.3390/atmos14020380>

Academic Editors: Xiaohong Yao, Jialiang Feng and Yujiao Zhu

Received: 8 January 2023

Revised: 6 February 2023

Accepted: 9 February 2023

Published: 15 February 2023



**Copyright:** © 2023 by the authors. Licensee MDPI, Basel, Switzerland. This article is an open access article distributed under the terms and conditions of the Creative Commons Attribution (CC BY) license (<https://creativecommons.org/licenses/by/4.0/>).

## 1. Introduction

The air pollution problem in China has attracted much attention in recent decades [1,2]. Air quality can be affected by both the emissions and meteorological conditions [3–8]. Many studies have evaluated the adverse effects of PM<sub>2.5</sub>, O<sub>3</sub>, SO<sub>2</sub>, NO<sub>2</sub>, and NO<sub>x</sub> on human health, including childhood asthma and premature death in Asia and the Yangtze River Delta [9–13]. Ozone has been proven to be a very important trace gas which has a significant impact on ambient air quality, atmospheric oxidation, global climate change, and stratospheric depletion [14–16]. Since the emission controls instituted in 2019, concentrations of PM<sub>2.5</sub>, SO<sub>2</sub>, and NO<sub>2</sub> have decreased, but not those of O<sub>3</sub>. Thus, understanding the meteorological impact on air pollution has become one of the top environmental issues [17–19].

A typhoon is a warm cyclonic vortex often accompanied by an obvious and strong downdraft in the peripheral region. The stable atmospheric structure is favorable for the generation and accumulation of pollutants. Previous studies have focused on the synoptic [20–25] and chemical mechanisms [26–29] of fine particle pollution (haze events) and ozone pollution caused by typhoons. Under different synoptic backgrounds, including the control of the subtropical highs, as well as the periphery of typhoon and sea land winds, typhoons could have a significant impact on the generation, maintenance, transmission, and other evolutionary processes of the ozone [30–34]. The meteorological conditions of strong sunlight in summer and autumn, affected by frequent typhoons, could increase O<sub>3</sub> concentrations. Under the control of the peripheral circulation of typhoon and the subtropical highs, stable sunny, hot, and dry conditions could result in O<sub>3</sub> pollution [35–37]. Chen et al. [38] investigated the positive and negative impacts of typhoons on tropospheric ozone based on 17 typhoons that landed in southern China from 2014 to 2018 and found that in the early stage of typhoon development (for example, from the day before the typhoon to the day after the typhoon), when the typhoon is 400–1500 km away, the near surface ozone will be enhanced, and the positive ozone anomaly is 10–20 ppbv higher than the background ozone level, on average. The maximum enhancement of ozone in the near surface layer occurs at the radial distance of 1100–1300 km from the typhoon center. As the typhoon approaches southern China, the impact of these systems is ozone reduction. Jiang et al. (2015) studied the changes in surface O<sub>3</sub>, NO<sub>2</sub>, CO, and meteorology in Xiamen and Quanzhou, along the southeast coast of China, affected by typhoon ‘Hagupi’ from 12 to 14 June 2014. They provided the observational evidence of ozone from the upper troposphere and lower stratosphere (UTLS) regions invaded by the typhoon being displaced to the surface air. The study showed that the downdraft around the typhoon had a substantial impact on the large-scale stratospheric tropospheric ozone transfer process [39]. Yue Haiyan et al. [40] selected the development of typhoon ‘Nida’ from 27 July to 2 August 2016, and analyzed the ozone concentration during the typhoon. Under adverse meteorological conditions, such as high temperature, low humidity, low wind speed, and the pressure equalization field, the atmospheric photochemical reaction was intense, which promoted the increase in local O<sub>3</sub> concentrations. In addition, affected by the downdraft around the typhoon, a lower mixing layer height and an ozone-benefiting sinking motion was determined. Moreover, the stable atmospheric structure made ozone diffusion and removal difficult. Chen Li et al. [41] used the reanalyzed data of the vertical ozone stratification in Central Europe and the total ozone column data to determine that the ozone concentration in the area most frequently affected by the strong updraft in the typhoon center is low, while the ozone concentration in the area most affected by the downdraft around the typhoon is high. This indicates that the cyclone over the northwest Pacific Ocean transports the air from the low level to the high level, bringing low concentration ozone to the typhoon center. Thus, the ozone concentration in the center of the typhoon decreased. On the contrary, the downdraft caused by the wind could transfer the high concentration of ozone in the upper layer to the near surface, resulting in a significant increase in the ozone concentration in the area affected by the typhoon. Many studies have developed a set of ozone data quality control schemes through numerical simulation [42–44] or retrieval of satellite data, such as FY-3A meteorological satellite [45–47], exploring the relationship between the ozone and the typhoon cloud top temperature, comparing the retrieval results with a variety of observation data.

The coastal cities in southeast China (CCSE) are often affected by typhoon systems; they have also experienced significant economic development and urbanization, accompanied by a large increase in air pollution [48,49]. Atmospheric conditions associated with typhoons, such as strong winds, dryness, lack of wind, high temperatures, and strong radiation, as well as variation in boundary layer height, vertical sinking transportation or regional transportation [30–40,50,51], may have a crucial impact on air quality in the region. Furthermore, the routes of typhoons affecting coastal areas of China are also different, which can be analyzed by individual case analysis or general course classification and

aggregation [38–40]. However, the research on the impact of typhoons passing the north-bound path along the southeast coast on the air quality in CCSE, especially the detailed analysis using ground-based and remote sensing observation methods, is still rare. The influence mechanism of typhoons on air pollution in the region is still unclear.

In this study, we investigated the annual and diurnal variation characteristics of air pollutants in CCSE affected by typhoons from 2019 to 2021. The process of the super typhoon 2114 ‘Chanthu’ moving northward in 2021 was selected as a the study case. Based on multi-source measurements, including ground-based observation and vertical profiles, the impact of TC<sub>N-SEC</sub> and the peripheral circulation on the air quality in the region was analyzed. The results illustrate the important impact of typhoons on air quality in CCSE and provide a scientific basis for regional air pollution control.

## 2. Data and Method

### 2.1. Typhoon Data

The CCSE region is delineated by a longitude from 117.5° E to 120.2° E, and a latitude from 23.8° N to 26.2° N (red box in Figure 1). Putian City (PT), Quanzhou City (QZ), and Xiamen City (XM) were selected to represent CCSE for the analysis of air quality (red dots in Figure 1). A target area (24.6° N to 34.4° N and 123.02° E to 132.92° E) was used in the study of TCN-SEC (Figure 1).

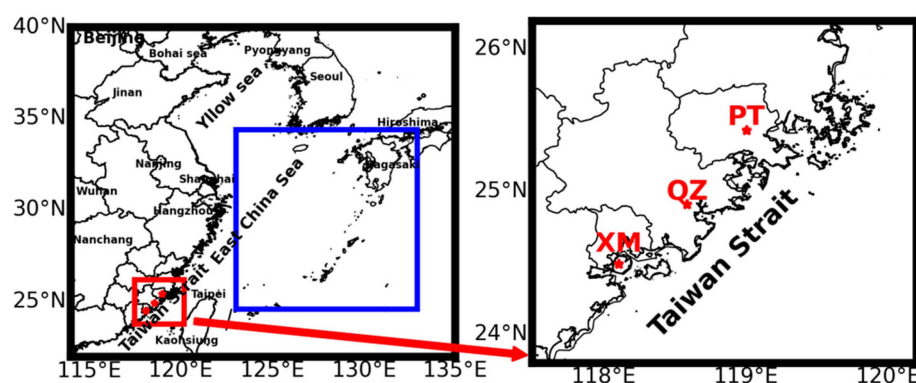


**Figure 1.** Maps of CCSE (red starts) and the target area of TC<sub>N-SEC</sub> (blue box).

In this paper, the statistics of the northward typhoons along the southeast coast of China (TCN-SEC) and the track data of the super typhoon 2114 ‘Chanthu’ in 2021 were all derived from the TC best-track dataset of the China Meteorological Administration (CMA)’s tropical cyclone (TC) database ([tcdata.typhoon.org.cn](http://tcdata.typhoon.org.cn) (accessed on 12 May 2022)) [52,53]. The date of TCN-SEC landing in the target area (DatesTC) are listed in Table 1. According to the frequencies of typhoons, this paper selected June to September, during 2019 to 2021, as the total statistical period (TSP), and analyzed the air quality during the TSP and DatesTC, respectively.

**Table 1.** List of the DatesTC and the corresponding location of the typhoon center.

| Year | Month | Day | Longitude (E, Degree) | Latitude (N, Degree) |
|------|-------|-----|-----------------------|----------------------|
| 2019 | 6     | 27  | 130.4                 | 28.5                 |
| 2019 | 7     | 19  | 124.1                 | 29                   |
| 2019 | 7     | 20  | 125.6                 | 34.2                 |
| 2019 | 8     | 6   | 130.6                 | 33                   |
| 2019 | 8     | 9   | 123.4                 | 26.5                 |
| 2019 | 8     | 15  | 132.5                 | 32.7                 |
| 2019 | 9     | 6   | 125                   | 28.1                 |
| 2019 | 9     | 8   | 125                   | 28.3                 |

**Table 1.** *Cont.*

| Year | Month | Day | Longitude (E, Degree) | Latitude (N, Degree) |
|------|-------|-----|-----------------------|----------------------|
| 2019 | 9     | 9   | 123.9                 | 31.8                 |
| 2019 | 9     | 21  | 125.7                 | 26.1                 |
| 2019 | 9     | 22  | 126.8                 | 30.8                 |
| 2019 | 10    | 2   | 123.9                 | 31.9                 |
| 2019 | 11    | 23  | 125.7                 | 25.2                 |
| 2019 | 11    | 24  | 126.5                 | 30                   |
| 2020 | 8     | 3   | 123.4                 | 25                   |
| 2020 | 8     | 10  | 127.6                 | 32.1                 |
| 2020 | 8     | 23  | 123.9                 | 26.3                 |
| 2020 | 8     | 24  | 126.2                 | 27.3                 |
| 2020 | 8     | 25  | 125.8                 | 29.1                 |
| 2020 | 8     | 26  | 124.5                 | 32.4                 |
| 2020 | 9     | 1   | 126.1                 | 26.9                 |
| 2020 | 9     | 2   | 126.9                 | 30.5                 |
| 2020 | 9     | 6   | 130.4                 | 27.7                 |
| 2020 | 10    | 8   | 132.8                 | 27.9                 |
| 2021 | 6     | 5   | 124                   | 24.9                 |
| 2021 | 7     | 24  | 124.6                 | 26.4                 |
| 2021 | 8     | 8   | 126.5                 | 29.1                 |
| 2021 | 8     | 4   | 124.6                 | 24.8                 |
| 2021 | 8     | 5   | 127.2                 | 26.2                 |
| 2021 | 8     | 6   | 131.7                 | 26.8                 |
| 2021 | 8     | 23  | 125.2                 | 29.1                 |
| 2021 | 9     | 13  | 123.6                 | 29.1                 |
| 2021 | 9     | 14  | 123.9                 | 31.3                 |
| 2021 | 9     | 15  | 125.7                 | 30.3                 |
| 2021 | 9     | 16  | 125.1                 | 30.5                 |
| 2021 | 9     | 17  | 127.5                 | 32.9                 |

## 2.2. Observation of Atmospheric Components

The surface observation data of atmospheric components ( $O_3$ ,  $PM_{10}$ ,  $PM_{2.5}$ ,  $NO_2$ ,  $SO_2$ ) in CCSE from June to September, during 2019 to 2021, are derived from the hourly air quality data released by the China National Environmental Monitoring Station (<https://air.cnemc.cn:18007/> (accessed on 18 January 2022)). Daily average concentrations ( $PM_{10}$ ,  $PM_{2.5}$ ,  $O_3$ ,  $NO_2$ ,  $SO_2$ , see Table 2) and objective statistical characteristic values for the period were calculated according to ambient air quality standard (GB3095-2012) and Technical Regulations on Ambient Air Quality Index (AQI) (Trial) (HJ633-2012). The ozone vertical distribution (Table 2) observed by ozone LIDAR (Differential Absorption Ozone Lidar, Wuxi Zhongke Optoelectronics Technology Co., Ltd., Wuxi, China) [54–56] at the Xiamen Environmental Monitoring Center Station in Fujian Province during the period from 13 September to 17 September 2021, with the time resolution of 12 min and vertical resolution of 7.5 m, is used in this study. According to the principle of ozone LIDAR, 266 nm and 289 nm are used to retrieve the  $O_3$  profile below 1000 m, and 289 nm and 316 nm are used to retrieve the  $O_3$  profile above 1000 m.

## 2.3. Meteorological Data

The measurements of the surface meteorology parameters (Table 2) are derived from the hourly operational observation data of the meteorological observation station in Xi'an District, Xiamen, Fujian Province (XMXAMOS). The air temperature (AirT), relative humidity (RH), and wind and rain data from the station from 13 September to 17 September 2021, are selected for the comprehensive analysis of meteorology parameters in the case study. Profiles of wind, relative humidity, depolarization ratio, and extinction coefficient (Table 1) are derived, respectively, using a microwave radiometer, a wind profiler, and an aerosol LIDAR at XMXAMOS from 13 September to 17 September 2021. As for the atmospheric boundary layer, 1500 m is selected as the highest value of the profiles in this

paper. RH profiles below 1500 m were observed from the 42-channel microwave radiometer (GRAW-RPG-HATPRO-G4, Shanghai Gelao Meteorological Instrument and Equipment Co., Ltd., Shanghai, China) [57], with a time resolution of 1 min. The vertical resolution of the microwave radiometer varies with the height, which is 25 m, 30 m, 40 m, and 60 m corresponding to the height below 100 m, between 100 m and 520 m, between 520 m and 1200 m, and between 1200 m and 1500 m, respectively. The wind profile with a height of 150 m~1500 m is selected from the low tropospheric wind profile radar (CFL-06L, Aerospace New Meteorological Technology Co., Ltd., Wuxi, China) [57,58], with a time resolution of 6 min and a vertical resolution of 120 m. The profiles of depolarization ratio (Dpr), the extinction coefficient (Ext) with a height of 75 m~1500 m, and the height of the pollution boundary layer were retrieved from Micro-Pulse Mie scattering polarization LIDAR (EV Lidar, Beijing Yifu Herong Technology Co., Ltd., Beijing, China) [59,60], with a time resolution of 1 min and a vertical resolution of 15 m.

**Table 2.** Overview of the multi-source measurements.

| Category                                     | Parameter  | Units   | Time               | Periods              |
|--|--|---|--------------------|----------------------|
| Observational data of atmospheric components | O <sub>3</sub> , PM <sub>10</sub> , PM <sub>2.5</sub> , NO <sub>2</sub> , SO <sub>2</sub>            | µg/m <sup>3</sup>   | LCT                | 2019–2021            |
|  | Ozone profile  | ppbv  | LCT                | 14–17 September 2021 |
| Measurements of meteorology                  | Air temperature (AirT), relative humidity (RH), wind and rain data                                   | AirT: °C<br>RH: %<br>Wind speed: m/s<br>Rain: mm<br>Horizontal wind speed: m/s    | UTC convert to LCT | 14–17 September 2021 |
|  | Wind profile   | Horizontal wind direction: °<br>Vertical velocity: m/s (+: upward, -: downward)   | UTC convert to LCT | 14–17 September 2021 |
|  | Relative humidity profile  | %   | UTC convert to LCT | 14–17 September 2021 |
|  | Profiles of depolarization ratio, extinction coefficient, and the height of pollution boundary layer | Extinction coefficient: Km <sup>-1</sup><br>Height of pollution boundary layer: m | LCT                | 14–17 September 2021 |

The weather situation charts were drawn using the fifth-generation reanalysis data ERA5 of the European Medium Range Weather Forecast Center (ECMWF, website: <https://cds.climate.copernicus.eu/> (accessed on 10 May 2022)) [61,62], with a resolution of 0.25° × 0.25°. Based on reanalysis data, hourly data on U, V components of the wind and geopotential height of 500 hPa, 700 hPa, 850 hPa, and 900 hPa, and total cloud cover are selected for comprehensive analysis of the individual weather processes in the target area of TC<sub>N-SEC</sub> during 13–17 September 2021.

### 3. Results

#### 3.1. Air Quality in CCSE Affected by the Typhoon

The annual average concentrations of air pollutants in CCSE during the TSP and Dates<sub>TC</sub> are shown in Figure 2. During the TSP, typhoons affected CCSE for an average of 10 days per year. The annual average concentrations of PM<sub>10</sub>, PM<sub>2.5</sub>, SO<sub>2</sub>, and NO<sub>2</sub> in CCSE during the TSP decreased year by year, while the O<sub>3</sub> concentration increased. Student's *t* test had been used to compare the annual average concentrations of air quality of CCSE during the TSP and the Dates<sub>TC</sub>. The results of Table S1 (Supplementary file) showed that the significant differences of O<sub>3</sub>, PM<sub>10</sub>, PM<sub>2.5</sub>, SO<sub>2</sub>, and NO<sub>2</sub> respectively in Figure 2 passed the significance test. The annual average concentration of air pollutants in CCSE during the



Dates<sub>TC</sub> ( $O_3$  (TC),  $PM_{10}$  (TC),  $PM_{2.5}$  (TC),  $SO_2$  (TC), and  $NO_2$  (TC)) were slightly higher than the annual average concentration of TSP, and the increase in  $O_3$  (TC) concentration was the most obvious. This indicated that since 2019, the TC<sub>N-SEC</sub> has had a positive impact on the increasing concentration of air pollutants in CCSE, especially regarding the increase in  $O_3$  concentrations.

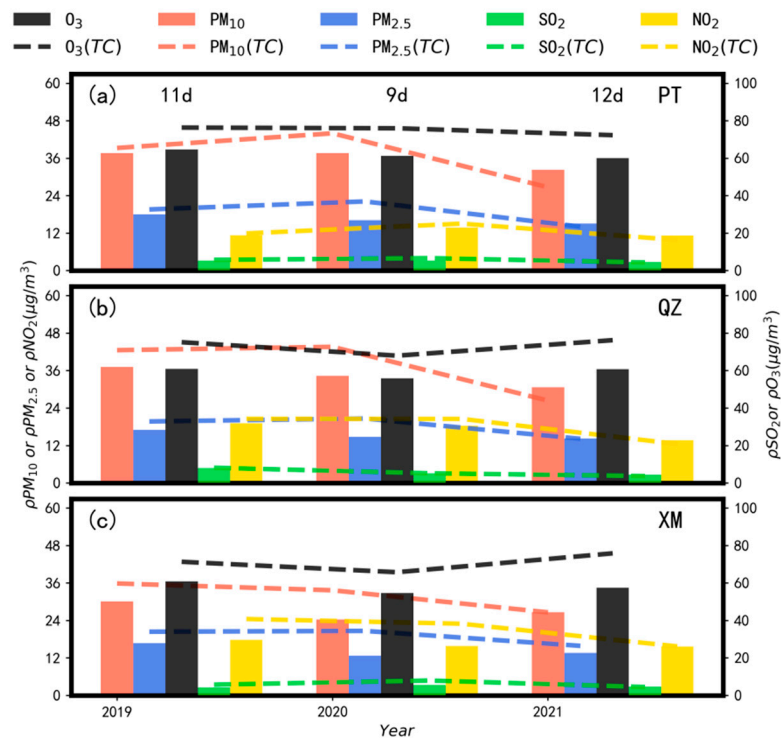


**Figure 2.** Comparison of the annual average concentrations of air pollutants in CCSE during the TSP (bars) and the Dates<sub>TC</sub> (dotted-lines). (a) Comparison of Putian City (b) Comparison of Quanzhou City (c) Comparison of Xiamen City.

The diurnal variations in air pollutants during the TSP, the Dates<sub>TC</sub>, and the noTC influenced period are shown in Figure 3. It can be seen that since 2019, the diurnal pattern of air pollutants in CCSE during Dates<sub>TC</sub> was similar with that during the TSP. The  $O_3$  concentrations in the three cities during the Dates<sub>TC</sub> were significantly higher than that during the TSP and non-typhoon (noTC) influenced period. For other air pollutants, different from PT and QZ, the diurnal variation trend of XM during the Dates<sub>TC</sub> was higher than that during the TSP and the non-typhoon influenced period, and  $\rho NO_2$  was particularly high. The differences showed that the TC<sub>N-SEC</sub> and peripheral circulation characteristics could increase  $O_3$  concentration in CCSE, and also that they had a comprehensive impact on the diurnal variation in  $PM_{10}$ ,  $PM_{2.5}$ ,  $SO_2$ , and  $NO_2$ .

### 3.2. Overview of the Impact of Super Typhoon 2114 ‘Chanthu’ on Air Quality in CCSE

The super typhoon 2114 ‘Chanthu’ was selected for detailed analysis of the impact of the typhoon on the air quality in CCSE. According to the method used in Section 2.1 13 September to 17 September 2021, was defined as the stage when the typhoon moved northward and affected CCSE, and the concentrations of the air pollutants are shown in Figure 4. During this period, the daily maximum concentrations of  $O_3$ ,  $PM_{10}$ ,  $PM_{2.5}$ ,  $SO_2$ , and  $NO_2$  in Xiamen were significantly higher than those exhibited during the TSP (Figure 3) and the average levels of each parameter during the TSP (Figure 2). The concentration and diurnal variation patterns of each pollutant from 14 September to 16 September was similar to the average values, and the diurnal fluctuation in these 3 days was relatively intense during the period. The daily maximum of  $PM_{10}$  and  $PM_{2.5}$  appeared at 11 h on 14 September ( $58.5 \mu g/m^3$  and  $35.5 \mu g/m^3$  respectively), and the  $O_3$  concentration peaked

at 14 h on 14 September ( $194.8 \mu\text{g}/\text{m}^3$ ). The daily maximum  $\text{SO}_2$  concentration was  $13.0 \mu\text{g}/\text{m}^3$  at 9 h on 15 September, and the daily maximum  $\text{NO}_2$  concentration was  $49.0 \mu\text{g}/\text{m}^3$  at 23 h on 13 September. In addition, it was worth noting that the daily minimum  $\text{O}_3$  concentration was  $15.0 \mu\text{g}/\text{m}^3$  at 5 h on 14 September, as the lowest value during the period. A detailed analysis will be provided in Section 3.3.3.

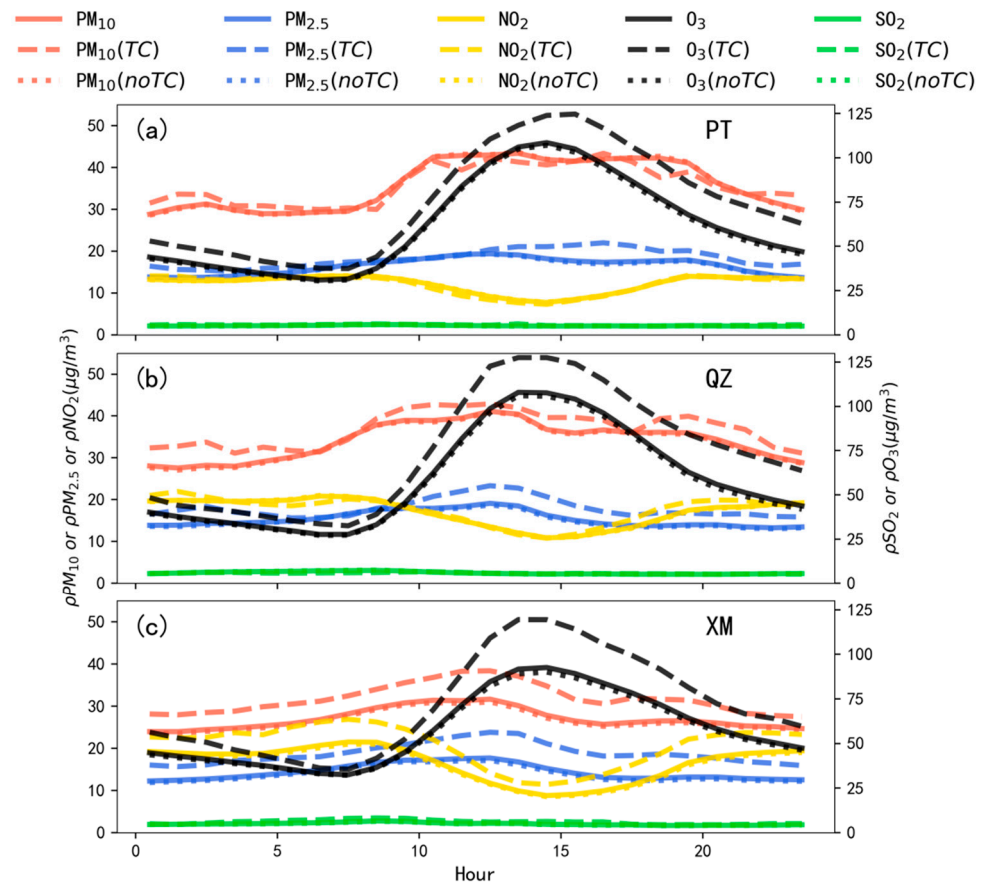


**Figure 3.** Comparison of diurnal variations in air pollutants during the TSP, the Dates<sub>TC</sub>, and the noTC-influenced period. (a) Comparison of Putian City (b) Comparison of Quanzhou City (c) Comparison of Xiamen City.

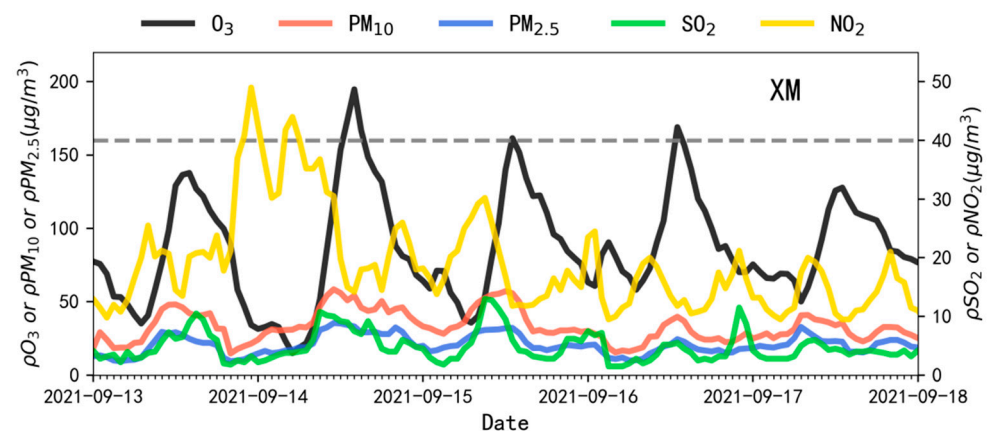


**Figure 4.** Time series of the concentrations of  $\text{PM}_{10}$ ,  $\text{PM}_{2.5}$ ,  $\text{O}_3$ ,  $\text{NO}_2$ , and  $\text{SO}_2$  in Xiamen from 13 September to 17 September 2021.

### 3.3. Comprehensive Analysis of Influencing Factors

#### 3.3.1. Weather Situation

From 13 to 17 September 2021, super typhoon 2114 ‘Chanthu’ moved northward into the target area of TC<sub>N-SEC</sub>. ‘Chanthu’ was located in the east of Shanghai and moved slowly, with an average speed of less than 5 km/h, and the intensity gradually weakened from 14 September to 15 September (Figure 5). The weather charts (Figure 6) showed relatively consistent northwest wind (4 to 12 m/s at 700–850 hPa) in Fujian Province at 500–850 hPa at 8 h on 14 September, with a weak convergence at 900 hPa. Affected by the cyclonic shear in the south of the typhoon, the surface temperature remained high, and the weather was cloudy, with the total cloud cover being 0.6–0.8.

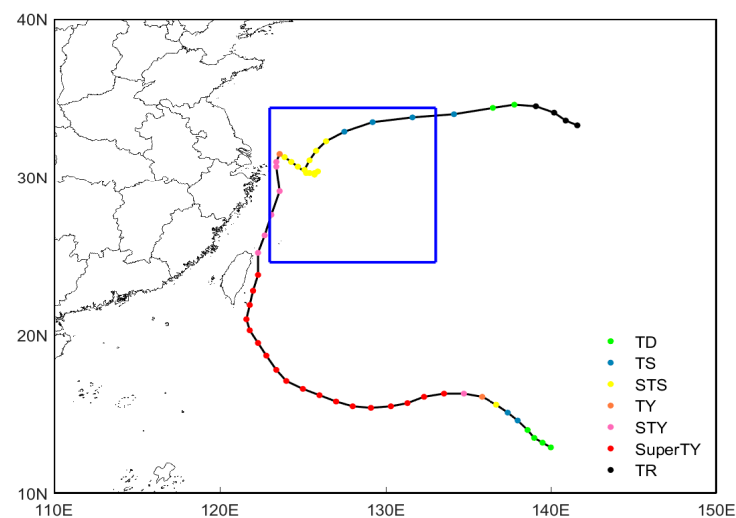


**Figure 5.** The best tracking and intensity chart for super typhoon 2114 ‘Chanthu’. Blue square represents the target area of TC<sub>N-SEC</sub>.

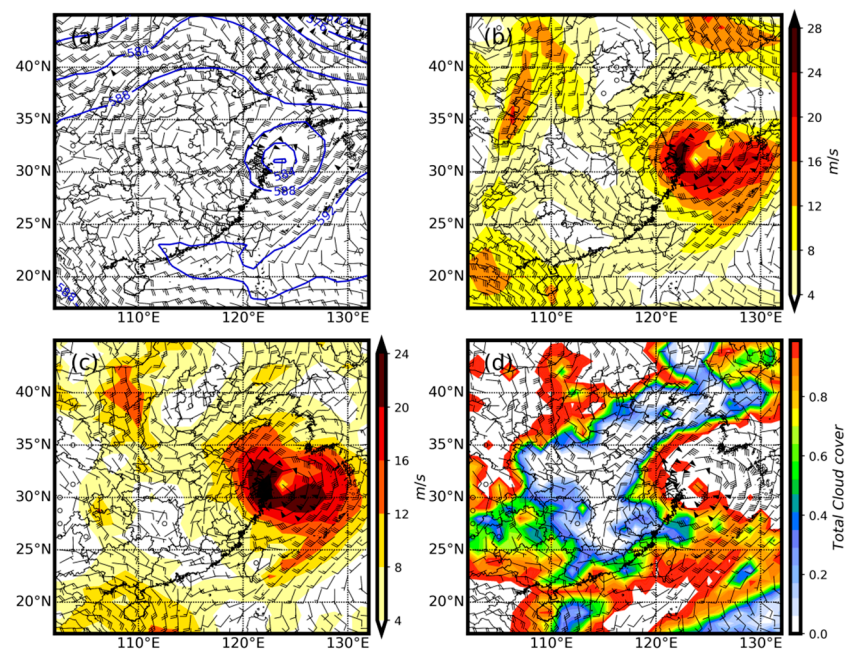


**Figure 6.** The 500–900 hpa weather chart at 8 h on 14 September 2021: (a) 500 hpaDagpm + 500 hpaWind, (b) 700 hpaWind, (c) 850 hpaWind, (d) 900 hpaWind+TCC).



### 3.3.2. Horizontal Diffusion Condition

Due to the influence of cyclonic shear in the south of the typhoon, there existed a weak convergence at the lower level. The prevailing north wind near the surface was found by analyzing the ground meteorological observation data of Xiamen Station (Figure 7), and the speeds during 2 min of wind varied greatly. During the period from 00h on 13 September to 23:59 on 17 September, the northerly wind speed fluctuated significantly between 0 m/s and 34.2 m/s. The wind speed fluctuated greatly before 0 h on 17 September, and dropped below 12.7 m/s. The frequency of the wind speed between 0 m/s and 0.2 m/s (calm) reached 14.6%, mainly at night and in the early morning, while the frequency of the wind speed greater than 13.9 m/s (moderate gale) reached 52.1%, mainly during daytime and nighttime precipitation before 0 h on 17 September. The air temperature showed a sinusoidal diurnal variation pattern of low at night and in the morning, with subsequent increases around noon, ranging from 25 °C to 35.1 °C. The daily maximum was higher than 31.8 °C, with the highest temperature of 35.1 °C occurring at 12 h on 14 September. The relative humidity was significantly negatively correlated with the air temperature, and the values higher than 80% accounted for 62.5% of all values during this period. The RH's diurnal changes (daily maximum RH minus daily minimum RH) ranged from 28% to 37%, with the maximum occurring on 14 September, followed by those on 15 September and 17 September. The minimum RH on 14 September was 56%, which appeared at 12 h. On the nights of the 13th and 14th, and during the early morning of the 16th, the accumulated precipitation was more than 0.5 mm. Thus, the horizontal transmission of the upwind atmospheric compositions brought by the moderate gale near the ground may have made a positive contribution to the significant increase in PM<sub>10</sub>, PM<sub>2.5</sub>, SO<sub>2</sub>, and NO<sub>2</sub> on 14 September and 15 September. However, the stable RH on 13 September, the relatively strong precipitation in the early morning of 16 September, and the significantly reduced wind speed on 17 September reduced the concentrations of PM<sub>10</sub>, PM<sub>2.5</sub>, SO<sub>2</sub>, and NO<sub>2</sub> on 13th September, 16 September, and 17 September. Calm and light air near the ground, weak precipitation, high humidity in the early morning and at night, the daily maximum temperature, and the minimum relative humidity could provide favorable meteorological conditions for the accumulation of O<sub>3</sub> precursors and the photochemical reaction during the daytime, playing a positive role in pushing the daily maximum O<sub>3</sub> on 14 September to 16 September to exceed 160 µg/m<sup>3</sup>. It is particularly noteworthy that the wind speed changed frequently between moderate gale, calm, and light air from 19 h on 13 September to 6 h on 14 September, with the maximum value of 34.2 m/s occurring at 21 h on 13 September. The precipitation at 19 h on 13 September was 0.5 mm, which was relatively weak compared with the accumulated precipitation during the night on 15 September and 16 September, and the effect of wet removal was weak. These conditions were more favorable in the early night from 13 September to 14 September, when PM<sub>10</sub>, PM<sub>2.5</sub>, SO<sub>2</sub>, and NO<sub>2</sub> increased due to the contribution of upwind transmission and the accumulation of near ground particulate matter and atmospheric pollutants. The RH from 0 h to 7 h on 14 September continued to be above 85%, and PM<sub>2.5</sub> and PM<sub>10</sub> continuously accumulated due to hygroscopic growth. With the constant reduction of the RH in the morning, the AirT continuously increased due to the enhanced radiation. The southerly wind near the ground increased from 11 h to 16 h, but the wind speed gradually weakened from 17 h to 23 h, which was unfavorable to the diffusion of PM<sub>2.5</sub> and PM<sub>10</sub>, resulting in the smaller fluctuation of particulate matter concentrations in the afternoon than in the previous two days. Combined with the O<sub>3</sub> precursors accumulated previously, these became more favorable conditions for photochemical reaction. The continuous generation of O<sub>3</sub>, along with the accumulation of low-level weak convergence, resulted in the peak of O<sub>3</sub> at 14 h.

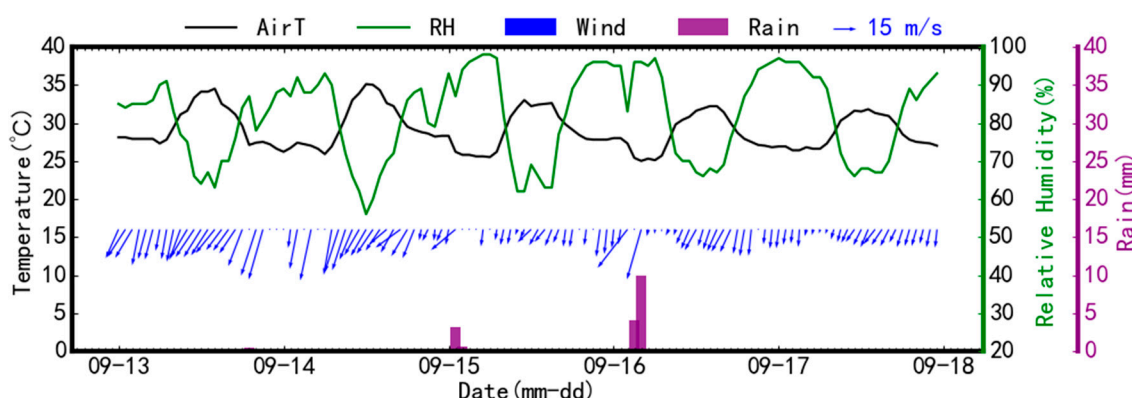


**Figure 7.** Time series of the measurements of rain, air temperature, wind direction, wind speed, and relative humidity at XMXAMOS from 14 September to 17 September 2021.

### 3.3.3. Vertical Diffusion Conditions

Affected by the peripheral circulation of the typhoon, the vertical wind field below 1500 m gradually turned to a north and east airflow from southerly and westerly airflow after 18 h on 14 September (Figure 8a). During the whole process, the vertical wind speed greater than 10 m/s mostly occurred at night and in the early morning. The wind speed below 1200 m was basically less than 6 m/s on 14 September, from 00:00 to 16:42. The large shift in the wind direction and speed during the night to early morning provided favorable conditions for the external transmission and local accumulation of atmospheric compositions. The time series of the RH profile (Figure 8a) demonstrated that the diurnal variation pattern of RH below 500 m was similar to that near the ground (Figure 7). The thickness of high RH (more than 80%) and average RH from the afternoon to early morning gradually decreased from 18 h on 14 September. The variations in RH within 1500 m during the process may contribute to the increase in the hygroscopicity of the aerosol particles and the nocturnal chemical reaction of  $\text{SO}_2$  and  $\text{NO}_2$ . The evolution of the light green layer, with the depolarization ratio between 0.05 and 0.1, can be clearly seen from the blue background [63] of the atmospheric molecules in general (Figure 8b). Compared with the background with a depolarization ratio of less than 0.05 on average, it was speculated that the light green layer may consist of relatively spherical aerosol particles, with a certain concentration formed after the hygroscopicity of the ultrafine particles [64] in the atmosphere, such as  $\text{PM}_{10}$  and  $\text{PM}_{2.5}$ . The light green layer increased with the development of the daytime pollution boundary layer, with the peak of the increase per day close to the height of the pollution boundary layer at noon. The average boundary layer height from 15 September to 16 September was relatively high, and the light green layer could increase up to 1000 m before noon, while it was lower than 1000 m on 14 September and 17 September. Dark red bands with depolarization ratio  $>0.15$  could also be seen from the night to the early morning of 13 September, 14 September, and 17 September, which was speculated to be a cloud layer. The height of the cloud base in the early morning of 14 September and 17 September was lower than 500 m, which inferred that the evolution of the pollution boundary layer can have a favorable impact on the local retention, accumulation, and diffusion of  $\text{PM}_{10}$  and  $\text{PM}_{2.5}$ , as well as the diurnal variation in  $\text{PM}_{10}$  and  $\text{PM}_{2.5}$  near the ground. A downdraft existed below 1000 m at night and in the early morning during the whole process, with the high extinction coefficient below 500 m (Figure 8c). In addition, the precipitation time on 14 September to 16 September also remarkably affected the extinction coefficient of the corresponding height. The extinction coefficient of the corresponding height of the depolarization ratio light green layer (Figure 8b) showed the deepening and lifting of the orange-red layer of  $0.6\sim 1.0\text{ km}^{-1}$ . The temporal distribution of  $\text{O}_3$  below 1500 m (Figure 8d) showed that there was an obvious increase in  $\text{O}_3$ , and the thick layer of higher  $\text{O}_3$  ( $>150\text{ ppbv}$ ) extended to 500 m around noon every day. Particularly, the  $\text{O}_3$  concentrations remained high on 14 September. The high concentration

( $O_3 > 200$  ppbv) appeared around noon and the thickness of the high  $O_3$  layer extended up to 800 m. According to the vertical velocity of the wind profile in Figure 8c, the downdraft and precipitation between 500–1000 m also correspond to the high  $O_3$  in the upper layer gradually decreasing, and the low  $O_3$  in the lower layer gradually increasing. It is speculated that the atmospheric movement below 1500 m played a notable role in the mixing and diffusion of  $O_3$  in the vertical direction. The horizontal stable wind field and vertical mixing may also play a significant role in the vertical distribution of  $O_3$  at night, based on the observed multi-profiles. Combined with the vertical velocity dotted line (Figure 8c,d) between 500–1300 m at 10 p.m. after sunrise, we can see the sinking of  $O_3$  distribution near the height of the daytime pollution boundary layer. The entrainment and sinking of  $O_3$  in the residual layer may play a complementary role in increasing and maintaining the  $O_3$  concentration below 1000 m, or even near the ground.

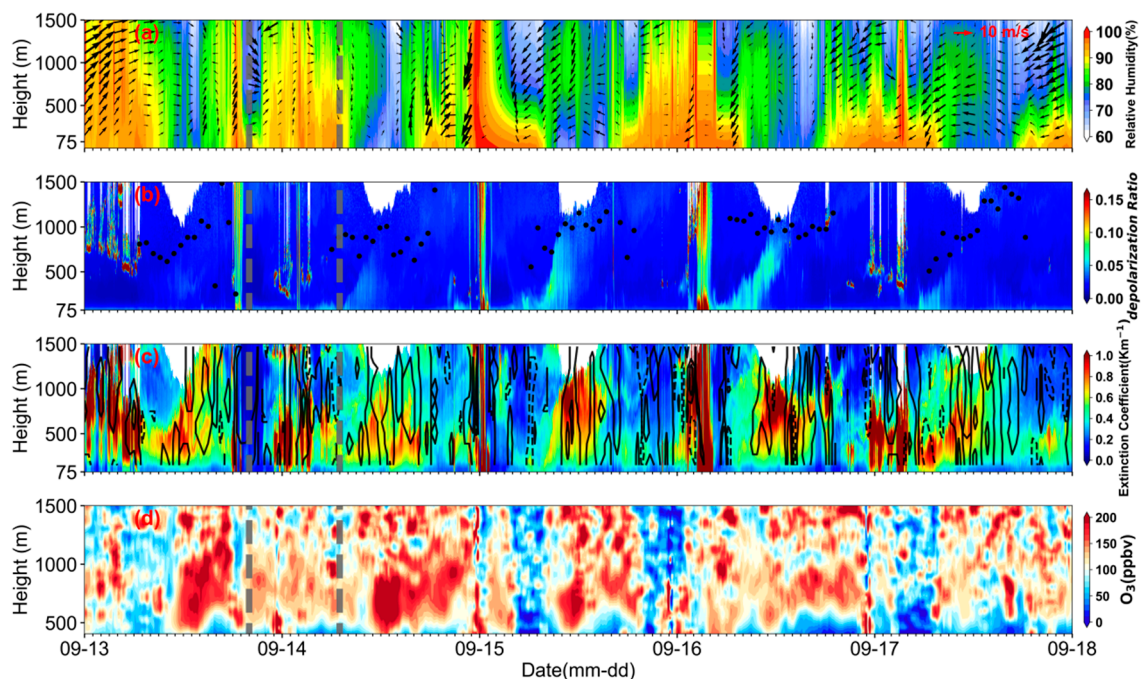


**Figure 8.** Time series of multi-source measurements of the profiles of wind, relative humidity, depolarization ratio, extinction coefficient, and ozone, and the height of the pollution boundary layer at XMAMOS from 14 September to 17 September 2021. (Black arrows on (a) represent the horizontal wind direction and speed. Black lines and dotted lines on (c) represent the vertical velocity of upward and downward wind directions, respectively. Black dots on (b) represent the height of the pollution boundary layer. (d) Temporal distribution of  $O_3$  profile).

The vertical evolution characteristics and impacts of various parameters analyzed over time can be mutually verified. Based on the statistical analysis results of surface observation, it was proved that the vertical and horizontal atmospheric structure significantly affected the variation characteristics of air quality in CCSE from 13 September to 17 September 2021, under the influence of super typhoon 2114 ‘Chanthu’.

#### 4. Conclusions

- (1) According to the comprehensive analysis of the air quality in CCSE during the typhoon prone period (June to September) from 2019 to 2021, the  $TC_{N-SEC}$  and its surrounding weather situation had a favorable impact on the increase in the pollutant concentrations in CCSE, especially on the increase in  $O_3$  concentration. The  $TC_{N-SEC}$  and its surrounding weather situation had an increasing influence on the hourly concentrations of  $O_3$  of CCSE, as well as a comprehensive impact on the diurnal variation in  $PM_{10}$ ,  $PM_{2.5}$ ,  $SO_2$ , and  $NO_2$  of CCSE.

- (2) Based on the analysis of air quality, weather situation, and surface meteorology parameters from 13 to 17 September 2021, it was shown that, affected by the cyclonic shear in the south of super typhoon 2114 ‘Chanthu’, the horizontal transmission of the upwind atmospheric compositions brought by the moderate gale near the ground may have positively contributed to the significant increase in PM<sub>10</sub>, PM<sub>2.5</sub>, SO<sub>2</sub>, and NO<sub>2</sub>. However, the mild diurnal variation in RH, the relatively strong precipitation, and the significantly reduced wind speed had a comprehensive weakening effect on the relatively low PM<sub>10</sub>, PM<sub>2.5</sub>, SO<sub>2</sub>, and NO<sub>2</sub> levels. Calm conditions near the ground, weak precipitation, high humidity in the early morning and at night, high daily maximum AirT, and low RH could provide favorable meteorological conditions for the accumulation of precursors of O<sub>3</sub> and photochemical reaction during the day, playing a positive role in regards to the O<sub>3</sub> peak on 14 September to 16 September. It was also suggested that the horizontal stable conditions may also play a significant role in the local accumulation of ozone.
- (3) Using a suite of air quality data and multi-source observations, the impact of vertical atmospheric structure on air quality was analyzed. It was suggested that the large daily shift in wind direction and speed from night to early morning provided favorable conditions for the external transmission and local accumulation of atmospheric compositions. The evolution of RH below 1500 m during the process may contribute to the increase in the hygroscopicity of aerosol particles and the nocturnal chemical reaction of SO<sub>2</sub> and NO<sub>2</sub>. The evolution of the pollution boundary layer can have a positive impact on the local retention, accumulation, or diffusion of PM<sub>10</sub> and PM<sub>2.5</sub>, as well as the daily differences in PM<sub>10</sub> and PM<sub>2.5</sub> near the ground. The atmospheric movement below 1500 m played a notable role in the vertical mixing and diffusion of O<sub>3</sub>. The entrainment and sinking motion of O<sub>3</sub> in the residual layer may play a complementary role in increasing and maintaining the O<sub>3</sub> concentration below 1000 m, or even near the ground.

**Supplementary Materials:** The following supporting information can be downloaded at: <https://www.mdpi.com/article/10.3390/atmos14020380/s1>.

**Author Contributions:** Conceptualization, F.L. and H.W.; formal analysis, Q.Z., A.X., J.Z. and H.Z.; investigation, F.L. and H.W.; methodology, A.X. and H.W.; resources, F.L., Y.J. and J.Z.; software, F.L., Q.Z., Y.J. and A.X.; supervision, H.W.; validation, Q.Z.; writing—original draft, F.L.; writing—review and editing, F.L., Q.Z. and H.W. All authors have read and agreed to the published version of the manuscript.

**Funding:** This research was funded by the Natural Science Foundation of Fujian Province (2021J01463; 2021J01453, 2022J01446, 2022J011082), the Environmental Protection Technology Project of Fujian Province Environmental Protection Technology Project (2021R002), the National Natural Science Foundation of China (42005139), and the Guided Foundation of Xiamen Science and Technology Bureau (3502Z20214ZD4004, 3502Z20214ZD4006, 3502Z20214ZD4008, 3502Z20214ZD4009).

**Institutional Review Board Statement:** Not applicable.

**Informed Consent Statement:** Not applicable.

**Data Availability Statement:** Not applicable.

**Conflicts of Interest:** The authors declare no conflict of interest.

## References

1. Asante, A.H.; Zhou, L.L.; Xu, X.L.; Tehzeeb, M. Progressing towards Environmental Health Targets in China: An Integrative Review of Achievements in Air and Water Pollution under the ‘Ecological Civilisation and the Beautiful China’ Dream. *Sustainability* **2021**, *137*, 3664.
2. Tang, M.; Ding, J.; Kong, H.; Bethel, B.J.; Tang, D. Influence of Green Finance on Ecological Environment Quality in Yangtze River Delta. *Int. J. Environ. Res. Public Health* **2022**, *19*, 10692. [[CrossRef](#)]
3. Global Burden of Disease (GBD). Global age-sex-specific fertility, mortality, healthy life expectancy (HALE), and population estimates in 204 countries and territories, 1950–2019: A comprehensive demographic analysis for the Global Burden of Disease Study 2019. *Lancet* **2020**, *396*, 1135–1159.



4. U.S. Environmental Protection Agency (USEPA). *Integrated Science Assessment (ISA) for Particulate Matter*; Report No. EPA/600/R-19/188; Center for Public Health and Environmental Assessment Office of Research and Development U.S. Environmental Protection Agency: Durham, NC, USA, 2019.
5. Donaldson, K.; Li, X.; MacNee, W. Ultrafine (nanometre) particle mediated lung injury. *J. Aerosol Sci.* **1998**, *29*, 553–560. [[CrossRef](#)]
6. Schwartz, J. The Distributed Lag between Air Pollution and Daily Deaths. *Epidemiology* **2000**, *11*, 320–326. [[CrossRef](#)] [[PubMed](#)]
7. Chen, R.; Zhao, Z.; Kan, H. Heavy smog and hospital visits in Beijing, China. *Am. J. Respir. Crit. Care Med.* **2013**, *188*, 1170–1171. [[CrossRef](#)]
8. Silva, R.A.; Adelman, Z.; Fry, M.; West, J.J. The Impact of Individual Anthropogenic Emissions Sectors on the Global Burden of Human Mortality due to Ambient Air Pollution. *Environ. Health Perspect.* **2016**, *124*, 1776–1784. [[CrossRef](#)]
9. Shah, A.S.V.; Langrish, J.P.; Nair, H.; McAllister, D.A.; Hunter, A.L.; Donaldson, K.; Newby, D.E.; Mills, N.L. Global association of air pollution and heart failure: A systematic review and meta-analysis. *Lancet* **2013**, *382*, 1039–1048. [[CrossRef](#)] [[PubMed](#)]
10. Lelieveld, J.; Evans, J.S.; Fnais, M.; Giannadaki, D.; Pozzer, A. The Contribution of Outdoor Air Pollution Sources to Premature Mortality on a Global Scale. *Nature* **2015**, *525*, 367–371. [[CrossRef](#)]
11. Shindell, D.; Faluvegi, G.; Seltzer, K.; Shindell, C. Quantified, localized health benefits of accelerated carbon dioxide emissions reductions. *Nat. Clim. Chang.* **2018**, *8*, 291–295. [[CrossRef](#)]
12. Qu, Z.; Wang, X.; Li, F.; Li, Y.; Chen, X.; Chen, M. PM<sub>2.5</sub>-Related Health Economic Benefits Evaluation Based on Air Improvement Action Plan in Wuhan City, Middle China. *Int. J. Environ. Res. Public Health* **2020**, *17*, 620. [[CrossRef](#)] [[PubMed](#)]
13. Qin, Y.; Li, J.; Gong, K.; Wu, Z.; Chen, M.; Qin, M.; Huang, L.; Hu, J. Double high pollution events in the Yangtze River Delta from 2015 to 2019: Characteristics, trends, and meteorological situations. *Sci. Total Environ.* **2021**, *792*, 148349. [[CrossRef](#)] [[PubMed](#)]
14. Team, C.W.; Pachauri, R.K.; Reisinger, A. Climate change 2007: Synthesis report. In *Contribution of Working Groups I, II and III to the Fourth Assessment Report of the Intergovernmental Panel on Climate Change*; IPCC: Geneva, Switzerland, 2007.
15. Cape, J.N. Surface ozone concentrations and ecosystem health: Past trends and a guide to future projections. *Sci. Total Environ.* **2008**, *400*, 257–269. [[CrossRef](#)] [[PubMed](#)]
16. Carter, C.A.; Cui, X.; Ding, A.; Ghanem, D.; Jiang, F.; Yi, F.; Zhong, F. Stage-specific, nonlinear surface ozone damage to rice production in China. *Sci. Rep.* **2017**, *7*, 44224. [[CrossRef](#)] [[PubMed](#)]
17. Li, G.; Wei, W.; Wei, F.; Cheng, S.; Wen, W.; Wang, G. Diurnal variations of ozone and its precursors and ozone formation potential of VOCs at the boundary of a coking plant during summer and autumn. *Chin. J. Environ. Eng.* **2014**, *8*, 1130–1138.
18. Fishman, J.; Creilson, J.K.; Parker, P.A.; Ainsworth, E.A.; Vining, G.G.; Szarka, J.; Booker, F.L.; Xu, X. An investigation of widespread ozone damage to the soybean crop in the upper Midwest determined from ground-based and satellite measurements. *Atmos. Environ.* **2010**, *44*, 2248–2256. [[CrossRef](#)]
19. Geng, C.; Wang, Z.; Ren, L.; Wang, Y.; Wang, Q.; Yang, W.; Bai, Z. Study on the Impact of Elevated Atmospheric Ozone on Crop Yield. *Res. Environ. Sci.* **2014**, *27*, 239–245.
20. Wang, T.; Cheung, V.T.; Lam, K.S.; Kok, G.L.; Harris, J.M. The characteristics of ozone and related compounds in the boundary layer of the South China coast: Temporal and vertical variations during autumn season. *Atmos. Environ.* **2001**, *35*, 35–46. [[CrossRef](#)]
21. Wang, T.; Kwok, J.Y. Measurement and analysis of a multiday photochemical smog episode in the Pearl River Delta of China. *J. Appl. Meteorol.* **2003**, *42*, 404–416. [[CrossRef](#)]
22. Huang, J.P.; Fung, J.C.; Lau, A.K.; Qin, Y. Numerical simulation and process analysis of typhoon-related ozone episodes in Hong Kong. *J. Geophys. Res. Atmos.* **2005**, *110*, D05301. [[CrossRef](#)]
23. Jiang, F.; Wang, T.; Wang, T.; Xie, M.; Zhao, H. Numerical modeling of a continuous photochemical pollution episode in Hong Kong using WRF chem. *Atmos. Environ.* **2008**, *42*, 8717–8727. [[CrossRef](#)]
24. Wu, M.; Fan, S.; Wu, D. The characteristics of atmospheric boundary layer during tropical cyclone process and its influence on air quality over Pearl River Delta region. *China Environ. Sci.* **2013**, *33*, 1569–1576.
25. Yan, R.E.; Ye, H.; Lin, X.; He, X.; Chen, C.; Shen, J.D.; Xu, K.E.; Zheng, X.; Wang, L. Characteristics and influence factors of ozone pollution in Hangzhou. *Acta Sci. Circumstantiae* **2018**, *38*, 1128–1136.
26. Shen, J.; Yang, T.S.; Yan, P.Z. Characteristics and causes of ozone pollution in Guangdong province. *Environ. Sci. Technol.* **2020**, *43*, 90–95.
27. Wei, X.; Liu, Q.; Lam, K.S.; Wang, T. Impact of Precursor Levels and Global Warming on Peak Ozone Concentration in the Pearl River Delta Region of China. *Adv. Atmos. Sci.* **2012**, *29*, 635–645. [[CrossRef](#)]
28. Zhang, Y.; Shao, K.; Tang, X. The Study of Urban Photochemical Smog Pollution in China. *Acta Sci. Nat. Univ. Pekin.* **1998**, *34*, 392–400.
29. Wei, X.; He, J.; Wang, A. Regulation mechanism of high ozone pollution under the influence of tropical cyclones. *Guangdong Meteorol.* **2010**, *32*, 32–34.
30. Wang, H.; Lyu, X.; Guo, H.; Wang, Y.; Zou, S.; Ling, Z.; Wang, X.; Jiang, F.; Zeren, Y.; Pan, W.; et al. Ozone pollution around a coastal region of South China Sea: Interaction between marine and continental air. *Atmos. Meas. Tech.* **2018**, *18*, 4277–4295. [[CrossRef](#)]
31. Zhao, D.; Xin, J.; Wang, W.; Jia, D.; Wang, Z.; Xiao, H.; Liu, C.; Zhou, J.; Tong, L.; Ma, Y.; et al. Effects of the sea-land breeze on coastal ozone pollution in the Yangtze River Delta, China. *Sci. Total Environ.* **2022**, *807*, 150306. [[CrossRef](#)]



32. Jiang, Z.; Li, J.; Lu, X.; Gong, C.; Zhang, L.; Liao, H. Impact of western Pacific subtropical high on ozone pollution over eastern China. *Atmos. Meas. Tech.* **2021**, *21*, 2601–2613. [\[CrossRef\]](#)
33. Deng, T.; Wang, T.; Wang, S.; Zou, Y.; Yin, C.; Li, F.; Liu, L.; Wang, N.; Song, L.; Wu, C.; et al. Impact of typhoon periphery on high ozone and high aerosol pollution in the Pearl River Delta region. *Sci. Total Environ.* **2019**, *668*, 617–630. [\[CrossRef\]](#) [\[PubMed\]](#)
34. Wang, H.; Lin, C.; Chen, X. Effects of weather condition on surface ozone distribution in FuZhou. *Ecol. Environ. Sci.* **2011**, *20*, 1320–1325.
35. Wang, Y.; Wang, Z.; Chen, X.; Wang, Z.; Fan, S.; Chen, D.; Wu, Q. Impact of typical meteorological conditions on air pollution over Pearl River Delta in autumn. *Acta Sci. Circumstantiae* **2017**, *37*, 3229–3239.
36. Zhan, C.; Xie, M.; Huang, C.; Liu, J.; Wang, T.; Xu, M.; Ma, C.; Yu, J.; Jiao, Y.; Li, M.; et al. Ozone affected by a succession of four landfall typhoons in the Yangtze River Delta, China: Major processes and health impacts. *Atmos. Meas. Tech.* **2020**, *20*, 13781–13799. [\[CrossRef\]](#)
37. Wang, T.; Xue, L.; Brimblecombe, P.; Lam, Y.F.; Li, L.; Zhang, L. Ozone pollution in China: A review of concentrations, meteorological influences, chemical precursors, and effects. *Sci. Total Environ.* **2017**, *575*, 1582–1596. [\[CrossRef\]](#)
38. Chen, Z.; Liu, J.; Cheng, X.; Yang, M.; Wang, H. Positive and negative influences of landfalling typhoons on tropospheric ozone over southern China. *Atmos. Chem. Phys.* **2021**, *21*, 16911–16923. [\[CrossRef\]](#)
39. Jiang, Y.C.; Zhao, T.L.; Liu, J.; Xu, X.D.; Tan, C.H.; Cheng, X.H.; Bi, X.Y.; Gan, J.B.; You, J.F.; Zhao, S.Z. Why does surface ozone peak before a typhoon landing in southeast China. *Atmos. Chem. Phys.* **2015**, *15*, 13331–13338. [\[CrossRef\]](#)
40. Yue, H.; Gu, T.; Wang, C.; Wu, D.; Deng, X.; Huang, J.; Wang, Y. Influence of typhoon Nida process on ozone concentration in Guangzhou. *Acta Sci. Circumstantiae* **2018**, *38*, 4565–4572.
41. Chen, L.; Guo, S.; Hu, T.; Gao, Y. Analyse on the ozone distribution pattern and the relationship with typhoon process in the Pacific Northwest. *J. Yunnan Univ. Nat. Sci. Ed.* **2017**, *39*, 810–819.
42. Yu, W.; Luo, X.; Fan, S.; Liu, J.; Feng, Y.; Fan, Q. Characteristics analysis and numerical simulation of a heavy pollution process in the pearl river delta. *Environ. Sci. Res.* **2011**, *24*, 645–653.
43. Wei, X.; Lin, J.; Wang, T. Numerical simulation and mechanism study of high ozone pollution in the Pearl River Delta caused by typhoon Begonia. In Proceedings of the Branch Venue of Urban Meteorological Fine Forecast and Service of the 28th Annual Meeting of the Chinese Meteorological Society, Xiamen, China, 2 November 2011; pp. 1–15.
44. Chen, D.; Su, T. Analysis on distribution characteristics of substances in TTL region during typhoon Matsa. *J. Meteorol. Sci.* **2016**, *36*, 760–769.
45. Huang, B.; Bai, J.; Liu, J.; Zhong, Z. Retrieval of clear sky atmospheric sounding profile around typhoon Rananim using infrared hyperspectral measurements. *J. Trop. Meteorol.* **2007**, *23*, 401–408.
46. Liu, Y.; Zou, X. Quality Control of FY-3A Total Column Ozone and Its Application in Typhoons Tembin (2012) and Isaac (2012). *Chin. J. Atmos. Sci.* **2014**, *38*, 1066–1078.
47. Tang, L.; Wei, M.; Sun, X.; Li, H. Analysis on cloud phase state of the typhoon saomai with MODIS data. *J. Trop. Meteorol.* **2010**, *26*, 790–794.
48. Li, L.; Hu, J.; Li, J.; Gong, K.; Wang, X.; Ying, Q.; Qin, M.; Liao, H.; Guo, S.; Hu, M. Modelling air quality during the EXPLORE-YRD campaign—Part II. Regional source apportionment of ozone and PM<sub>2.5</sub>. *Atmos. Environ.* **2021**, *247*, 118063. [\[CrossRef\]](#)
49. Ozone Pollution Control Committee of Chinese Academy of Environmental Sciences. *China's Blue Book on the Prevention and Control of Atmospheric Ozone Pollution*, 2020 ed.; Science Press: Beijing, China, 2020.
50. Lang, S.; Tao, D.; Zhen-Ning, L.; Chen, W.; Guo-Wen, H.; Fei, L.; Meng, W.; Dui, W. Retrieval of Boundary Layer Height and Its Influence on PM<sub>2.5</sub> Concentration Based on Lidar Observation over Guangzhou. *J. Trop. Meteorol.* **2021**, *27*, 303–318. [\[CrossRef\]](#)
51. Li, L.; He, Y.; Lan, Z.; Li, Y.; Yang, H.; Fang, S. Environmental meteorological characteristics of ozone pollution in Shenzhen. *Acta Sci. Circumstantiae* **2023**, *43*, 109–118.
52. Ying, M.; Zhang, W.; Yu, H.; Lu, X.; Feng, J.; Fan, Y.; Zhu, Y.; Chen, D. An Overview of the China Meteorological Administration Tropical Cyclone Database. *J. Atmos. Ocean Technol.* **2014**, *31*, 287–301. [\[CrossRef\]](#)
53. Lu, X.; Yu, H.; Ying, M.; Zhao, B.; Zhang, S.; Lin, L.; Bai, L.; Wan, R. Western North Pacific Tropical Cyclone Database Created by the China Meteorological Administration. *Adv. Atmos. Sci.* **2021**, *38*, 690–699. [\[CrossRef\]](#)
54. Papayannis, A.; Ancellet, G.; Pelon, J.; Mégie, G. Multi-wavelength lidar for ozone measurements in the troposphere and the lower stratosphere. *Appl. Opt.* **1990**, *29*, 467–476. [\[CrossRef\]](#)
55. Cao, K.F.; Huang, J.; Hu, S.X. Investigation of stimulated Raman scattering characteristics in D<sub>2</sub>, H<sub>2</sub> and D<sub>2</sub>/H<sub>2</sub> mixtures. *Acta Opt. Sin.* **2015**, *35*, 0319001.
56. Li, Y.T.; Sun, T.L.; He, L. Vertical distribution characteristics of ozone pollution in Shenzhen in autumn. *China Environ. Sci.* **2020**, *40*, 1975–1981.
57. Jiang, Y.C.; Zhang, H.Y.; Zhang, W. Analysis of urban boundary layer characteristics based on ground-based remote sensing data in Xiamen. *Acta Sci. Circumstantiae* **2020**, *40*, 450–458.
58. Wang, Y.; Zhang, W.; Zhao, Y. Analysis of Wind Characteristics of Wind-Profiler Radars and Their Quality Control Methods for Data Assimilation. *Chin. J. Atmos. Sci.* **2021**, *45*, 123–147. (In Chinese) [\[CrossRef\]](#)
59. Jiang, Y.C.; Zheng, H.; Jiang, Z.X.; Jiang, Y.; Zheng, H.; Jiang, Z.; Chen, S.; Chen, D.; Zhao, T.; Wang, H.; et al. Study on spring particle matter pollution in coastal cities over West Bank of Taiwan Strait based on multi-source observations. *Acta Sci. Circumstantiae* **2018**, *38*, 1739–1750.

60. Xu, D.; Cao, P.; Wang, Y. Study of the Vertical Distribution of Aerosol Optical Properties During a Heavy Pollution Event in Chengdu. *Meteorol. Mon.* **2020**, *46*, 948–958. [[CrossRef](#)]
61. Hersbach, H.; Bell, B.; Berrisford, P.; Hirahara, S.; Horanyi, A.; Muñoz-Sabater, J.; Nicolas, J.; Peubey, C.; Radu, R.; Schepers, D.; et al. The ERA5 global reanalysis. *Q. J. R. Meteorol. Soc.* **2020**, *146*, 1999–2049. [[CrossRef](#)]
62. Hoffmann, L.; Günther, G.; Li, D.; Stein, O.; Wu, X.; Griessbach, S.; Heng, Y.; Konopka, P.; Müller, R.; Vogel, B.; et al. From ERA-Interim to ERA5: The considerable impact of ECMWF's next-generation reanalysis on Lagrangian transport simulations. *Atmos. Chem. Phys.* **2019**, *19*, 3097–3124. [[CrossRef](#)]
63. Gobbi, G.P. Polarization Lidar return from aerosols and thin clouds: A framework for the analysis. *Appl. Opt.* **1998**, *37*, 5505–5508. [[CrossRef](#)]
64. Bian, Y.X.; Zhao, C.S.; Ma, N.; Chen, J.; Xu, W.Y. A study of aerosol liquid water content based on hygroscopicity measurements at high relative humidity in the North China Plain. *Atmos. Chem. Phys.* **2014**, *14*, 6417–6426. [[CrossRef](#)]

**Disclaimer/Publisher's Note:** The statements, opinions and data contained in all publications are solely those of the individual author(s) and contributor(s) and not of MDPI and/or the editor(s). MDPI and/or the editor(s) disclaim responsibility for any injury to people or property resulting from any ideas, methods, instructions or products referred to in the content.